Tribology Letters (2018) 66:90
https://doi.org/10.1007/s11249-018-1042-x

ORIGINAL PAPER

Instantaneous Plane Stress Observation and Numerical Simulation During Wear in an Initial Line Contact

Wanglong Zhan[1] · Yanfei Fang[2] · Cuong Van Hoang[1] · Ping Huang[1]

Received: 26 April 2018 / Accepted: 13 June 2018 / Published online: 21 June 2018

Abstract
The photoelastic technique was applied to capture in situ plane stress in a block-on-cylinder contact. This method allows researchers to qualitatively visualize the distribution of principal stress difference during wear processes. Additionally, numerical simulation of the evolution of wear was conducted. The conjugate gradient method together with fast Fourier transform was employed to solve the pressure distribution. Based on the computed pressure, the block wear was solved with Archard's wear law. The subsurface stress was computed using the influence coefficient method. The simulated results of wear and stress were compared with the experimental results; the similarities and differences between the results highlight the usefulness and limitations of the numerical method. However, the photoelastic technique together with the numerical method casts light on the nature of wear.

Keywords Wear · Photoelasticity · Plane stress · Line contact

Nomenclature

d	Thickness of a birefringence specimen
E^*	Equivalent Young's modulus,$1/E^* = \left(1-\nu_1^2\right)/E_1 + \left(1-\nu_2^2\right)/E_2$
f_σ	Material stress fringe value
G^*	Equivalent shear modulus, $1/G^* = \left(1-2\nu_1\right)/G_1 - \left(1-2\nu_2\right)/G_2$
g	Gap between two contact bodies
g^0	Initial gap between two contact bodies
I_c	The set of all nodes that are in contact
I_g	The set of all nodes in the calculation domain
k	Wear coefficient
p	Normal pressure distribution
P	External normal loads
q	Tangential pressure distribution, $q=\mu p$
s	Total sliding distance
$\bar{u_z}$	Elastic deformation along the z direction
x, z	Spatial coordinates
$x_{1,2}$	Domain of contact
Δh	Wear depth increment
Δs	Sliding distance increment
Δx	The size of one mesh grid
δ	'rigid-body' approach
$\sigma_{x,z}$, τ_{zx}	Stress component

✉ Wanglong Zhan
zhanwl1992@foxmail.com

[1] School of Mechanical and Automotive Engineering, South China University of Technology, Guangzhou 510640, China

[2] State Key Laboratory of Tribology, Tsinghua University, Beijing 100084, China

1 Introduction

Wear is a widespread phenomenon in friction pairs with relative motion. It has been reported that wear failure accounts for approximately 60–80% of the total failure of mechanical pairs and components. Predicting wear and the risk of scuffing in friction pairs is essential to enhancing machine designs and predicting service life. Moreover, in situ investigations concerning the evolution of the maximum shear stress in the subsurface will allow us to better understand wear failure mechanisms.

According to the maximum shear stress theory, failure occurs when the maximum shear stress from a combination of principal stresses equals or exceeds the value of the maximum shear stress at yielding in uniaxial tension. Marshall et al. [1] and Hu et al. [2] introduced the concept of an instantaneous cohesive-length scale that describes the nature of stress fields around corners and defines when linear elasticity and Coulomb friction can provide an accurate description of the interfacial behavior. However, there is limited research on the value and position of the maximum

shear stress in the case of line contact during wear processes. Thus, the combination of numerical simulation and in situ plane stress observation during wear enables us to master the processes of stress evolution and wear mechanisms.

Optical methods such as photoelasticity are useful experimental techniques that enable researchers to obtain strain and stress information on a specimen surface or an area of interest. The photoelastic technique relies on birefringent materials, which have a unique optical property wherein two refracted rays will be observed when a single ray of light is incident on the material's surface. Photoelastic patterns provide information about the principal stress difference and the principal direction. With the growth of material processing techniques, preparing birefringent materials such as epoxy resin and polycarbonate becomes easier and less expensive. Thus, transmission photoelasticity has been extensively used to explore stress distribution. Dally and Chen [3] studied the friction of multipoint contacts using photoelasticity and introduced an overdeterministic method to obtain normal and tangential forces associated with isochromatic patterns. Bryant and Lin [4] developed a photoelastic technique to observe contact interfaces with and without sliding. Burguete and Patterson [5] studied the 3D stress distribution between a cylinder and a half-space using stress freezing. More recently, Fang et al. [6] applied this technique to study elastohydrodynamic lubrication.

Although the photoelastic pattern can qualitatively show the stress distribution beneath the contact surface, it is impossible to obtain stress components directly. There are several techniques for the analysis of fringe patterns [7–10]. However, these methods are mainly used in static contact. Therefore, fringe pattern analyses will be greatly complemented by the use of numerical simulations [11, 12]. Hundreds of wear equations have been developed to simulate wear processes for different conditions [13]. However, Archard's wear law is the best-known and widely used model [14]. The major difficulty in simulating wear is computing pressure distribution for arbitrary profiles during contact. To overcome these difficulties, several methods, such as the finite element method [15–18], the Winkler surface model [19, 20], and the boundary element method [21], have been employed. These methods are either time-consuming or inaccurate. The conjugate gradient method (CGM) [22], which converges for arbitrary rough surfaces, together with fast Fourier transform is a good choice to solve the pressure distribution due to its comparatively high speed of convergence and explicit iteration format.

In this paper, photoelasticity was employed to capture the instantaneous isochromatic fringe during wear in a line contact. Numerical simulations of the evolution of wear and pressure distribution were also conducted. Archard's wear law was used to calculate the wear volume, and the CGM algorithm was used to calculate the contact pressure. Moreover, the subsurface stresses were computed. The photoelastic technique together with the numerical method casts light on the nature of wear.

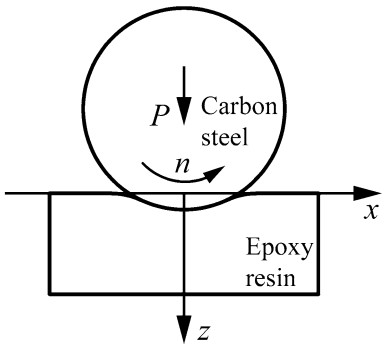

Fig. 1 Schematic diagram of line contact

2 Wear Simulation

2.1 Basic Equation

The wear model of a line contact is shown in Fig. 1. According to contact theory [23], the elastic deformation on the surface induced by normal and tangential tractions was expressed by

$$\bar{u}_z = -\frac{2}{\pi E^*}\int_{x_1}^{x_2} p(x')\ln|x-x'|\mathrm{d}x' - \frac{1}{2G^*}\int_{x}^{x_2} q(x')\mathrm{d}x' + C, \tag{1}$$

where E^* and G^* are the equivalent Young's modulus and shear modulus, respectively, C is a constant, and $[x_1, x_2]$ is the region of tractions.

Wear occurs from relative sliding between two counterparts. Physically, wear is caused by frictional work, which is proportional to the tangential traction and the sliding distance. However, Archard introduced an experimental wear coefficient k that indirectly includes the tangential effect. In Archard's wear law, which is widely accepted and reasonably concise, wear depth is considered proportional to normal pressure and sliding distance. It is expressed as

$$\Delta h = kp\Delta s, \tag{2}$$

where Δh is the wear depth, k is the wear coefficient, p is the normal pressure, and Δs is the relative sliding distance. Additionally, when the contact pressure is known, the subsurface stress field for plane strain conditions is expressed as

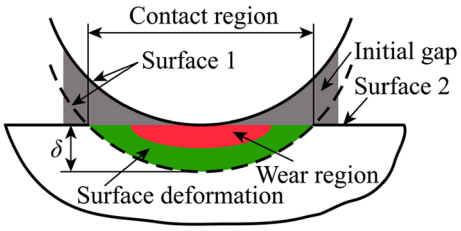

Fig. 2 Schematic diagram of the gap between the two contact surfaces ($g=0$ in the contact region)

where g is the gap between the two contact surfaces, P is the external normal loads, $\bar{u_z}$ is the surface normal displacement, Δx is the discretization size, $g_0=x^2/2R$ is the initial gap, h is the total wear depth, and δ is the 'rigid-body' approach of the two solids; the superscript represents the time discrete point and the subscript represents the spatial. The diagram of the gap is shown in Fig. 2.

The iteration scheme based on the CGM was employed to solve the discrete contact problem (5). Additional information about the CGM can be found in Ref. [22].[1] The nodal displacements $\bar{u_{zi}}$ produced by the corresponding contact

$$\begin{aligned}
\sigma_x &= -\frac{2z}{\pi}\int_{x_1}^{x_2}\frac{p(x')(x-x')^2}{\{(x-x')^2+z^2\}^2}\mathrm{d}x' - \frac{2}{\pi}\int_{x_1}^{x_2}\frac{q(x')(x-x')^3}{\{(x-x')^2+z^2\}^2}\mathrm{d}x' \\
\sigma_z &= -\frac{2z^3}{\pi}\int_{x_1}^{x_2}\frac{p(x')}{\{(x-x')^2+z^2\}^2}\mathrm{d}x' - \frac{2z^2}{\pi}\int_{x_1}^{x_2}\frac{q(x')(x-x')}{\{(x-x')^2+z^2\}^2}\mathrm{d}x' \\
\tau_{zx} &= -\frac{2z^2}{\pi}\int_{x_1}^{x_2}\frac{(x-x')p(x')}{\{(x-x')^2+z^2\}^2}\mathrm{d}x' - \frac{2z}{\pi}\int_{x_1}^{x_2}\frac{q(x')(x-x')^2}{\{(x-x')^2+z^2\}^2}\mathrm{d}x'.
\end{aligned} \tag{3}$$

The principal stress difference τ is expressed as

$$\tau = \sigma_1 - \sigma_2 = \sqrt{(\sigma_x-\sigma_z)^2+4\tau_{zx}^2}. \tag{4}$$

2.2 Numerical Procedure for Normal Pressure

It is known that the wear depth and the subsurface stress field are related to the contact pressure according to the description in Sect. 2.1. However, many non-Hertzian contact problems rarely permit closed-form analytical solutions. This is particularly true in the case of wear, where the contact shape cannot be described by a simple quadratic expression because it varies with time. Numerical methods are well suited for determining the contact pressure. A calculation domain $[x_1, x_2]$ is selected and uniformly divided into N elements. The nodes of the grid used in the contact analysis are denoted by i ($0\le i\le N$). The set of all nodes in the grid is marked by I_g. It should be noted that the calculation domain must be large enough to include all contact regions after wear.

The elastic contact problem based on the material removal can be described by the following equations and constraints:

$$\begin{cases}
p_i^j > 0,\ g_i^j = 0 \ (i\in I_c) \\
p_i^j = 0,\ g_i^j > 0 \ (i\notin I_c) \\
\Delta x\sum p_i^j = P \ (i\in I_g) \\
g_i^j = g_0 + h_i^j + (\bar{u}_z)_i^{j-1} - \delta_i^j \ (i\in I_g),
\end{cases} \tag{5}$$

pressure p_i and q_i are computed at each iteration step. Equation (1) gives the integral form expression to solve the surface normal displacement. However, the equation is a singular integral, and it should be expressed in a discrete form. Assuming that the Coulomb friction law is satisfied between normal and tangential tractions, i.e., $q=\mu p$, the relationship between surface normal displacements and traction can be written as

$$\bar{u}_{zi} = -\sum_j K_{i-j}p_j \quad (i,j\in I_g), \tag{6}$$

where K_{i-j} is the influence coefficient. The traction distribution is approximated by a stepwise constant function, which is uniform within each discrete element of the surface. Following this approximation, the influence coefficients K_{i-j} are calculated as delineated in Appendix A.

After obtaining the contact pressure, the wear depth increments can be solved using Eq. (2); the total wear depth is the sum of the wear depth increments. Furthermore, after the contact pressure is solved, the subsurface stress field would be obtained using the discrete form of Eq. (3), which can be written as follows:

$$\sigma_{rs}(x_i,z_k) = \sum_{j=0}^{N} N_{i-j}^{rs}(z_k)p_j + \sum_{j=0}^{N} T_{i-j}^{rs}(z_k)q_j, \tag{7}$$

[1] There is a typo in Eq. (31b) of the reference; it should be $p_{ij}\leftarrow(P_0/P)p_{ij}$.

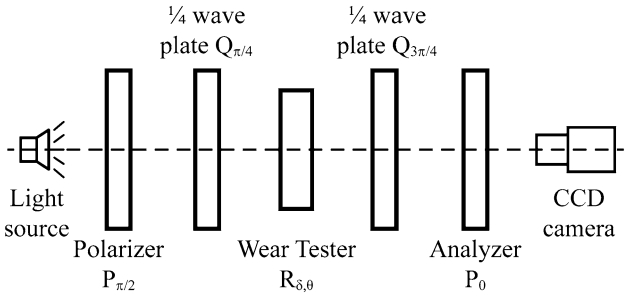

Fig. 3 Optical arrangement for photoelasticity

where $N_{i-j}^{rs}(z_k)$ and $T_{i-j}^{rs}(z_k)$ are the stress influence coefficients of the node i at the depth z_k for the normal traction p_j and the tangential traction q_j, respectively. The explicit formulas for $N_{i-j}^{rs}(z_k)$ and $T_{i-j}^{rs}(z_k)$ could be obtained by making an assumption of the stepwise uniform distribution of contact pressure; the details can be found in Appendix B.

As the numerical results are to be compared with the experimental data described in Sect. 3.2, a specific movement is necessary. Our simulation employed a sliding distance increment $\Delta s = 25$ mm to calculate the wear.

3 Experimental Details

3.1 Photoelasticity Method

A typical optical setup for photoelasticity, which is used to analyze isochromatic patterns, is shown in Fig. 3. This setup consists of a monochromatic light source, two linear polarizers, two quarter-wave plates, a CCD camera, and a birefringent specimen that experiences wear under preloads. A monochromatic light passes through a polarizer $P_{\pi/2}$ whose optical axis is vertical. Then, the linearly polarized light passes through the first quarter-wave plate $Q_{\pi/4}$, the fast axis of which subtends an angle of π/4 with a reference axis ox. The light emitted from the first quarter-wave plate becomes a circularly polarized light. The beam emitted from the first quarter-wave plate passes through a birefringent specimen with retardation δ, the fast axis of which makes an angle θ with the ox axis, the second quarter-wave plate $Q_{3\pi/4}$, an analyzer P_0, the optical axis of which is horizontal, and a CCD camera.

The light emerging from the analyzer can be derived using the Jones calculus [24]. The Jones vector E_d can be written as

$$E_d = P_0 Q_{3\pi/4} R_{\delta,\theta} Q_{\pi/4} P_{\pi/2}. \tag{8}$$

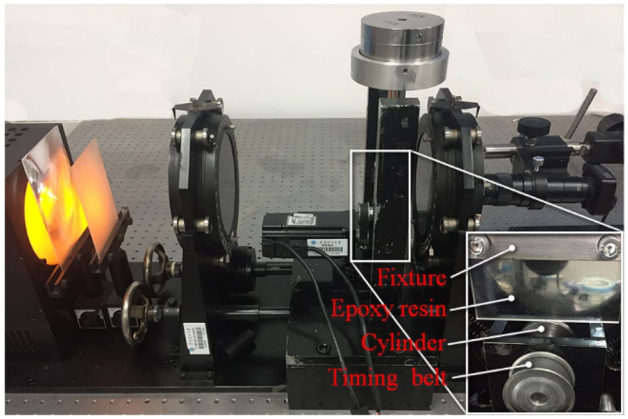

Fig. 4 Experimental setup

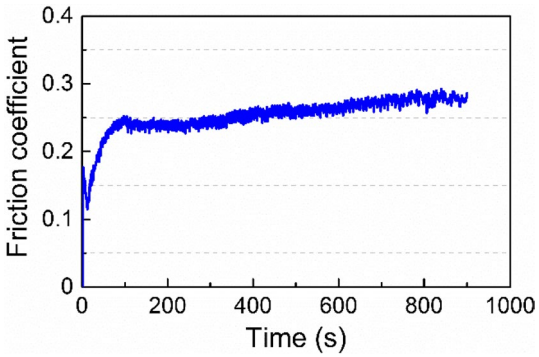

Fig. 5 Variations in the friction coefficients with time

The light intensity I_d is the product $E_d E_d^*$, where E_d^* denotes the complex conjugate E_d. Therefore, the light intensity can be expressed as

$$I_d = I_a \sin^2 \frac{\delta}{2}, \tag{9}$$

where I_a denotes the amplitude of the incident light vector. Meanwhile, the retardation δ of the specimen is related to the principal stress difference as [24]

$$\sigma_1 - \sigma_2 = \frac{\delta f_\sigma}{2\pi d}, \tag{10}$$

where f_σ is the material stress fringe value, which depends on the birefringent material and incident light wavelength, and d is the thickness of a specimen. The material stress fringe value can be measured using pure bending beam experiments [6] or disks under diametral compression tests [25].

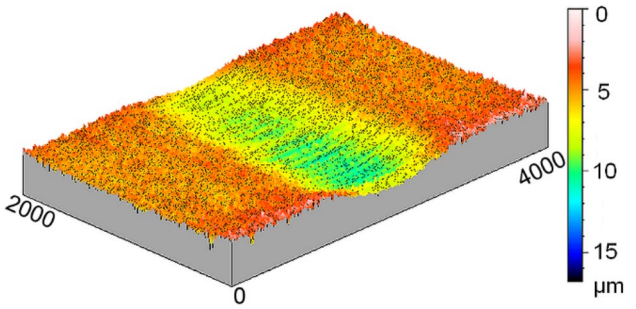

Fig. 6 3D wear scar of the epoxy resin

3.2 Experiment

Figure 4 shows the experimental setup for this work. A transparent block made of epoxy resin, 60 mm in width, 40 mm in height, and 4 mm in thickness, is subjected to the constant normal load of $P = 44$ N. These configurations enable the block to approximate a plane stress state without causing too much plastic deformation and can make the photoelastic patterns in the observation domain not too dense and too sparse. The material fringe value f_σ of the specimen is determined to be 14.6 kN/(m·fringe) by a four-point bending test. The cylinder–block wear tester, as shown in the inset, is placed in a circular polariscope. The diameter of the carbon steel cylinder is 49.22 mm, and the rotation speed is 100 r/min, which enables the camera to capture pictures more clearly without making the experiment consume too much time. The Young's modulus and Poisson's ratio are 2.1 GPa and 0.4, respectively, for the block and 210 GPa and 0.3, respectively, for the cylinder. A 587-nm-wavelength monochromatic light emitted from a low-pressure sodium lamp is used as the light source. The photoelastic patterns are collected by a CCD camera with a resolution of 659×494 pixels.

The experiments were conducted at room temperature under dry friction conditions. Prior to the photoelastic experiment, the friction coefficient between the epoxy resin and carbon steel was measured by a ring–block wear tester. The variation in the friction coefficient with time is shown in Fig. 5. After running in, the friction coefficient maintained a constant value of approximately 0.25. The wear scars of the specimen under a desired sliding distance were measured by a three-dimensional surface profilometer (Talysurf CLI 1000, Talyor Hobson). The wear coefficient k could be determined as [12]

$$k = \frac{V}{Ps}, \tag{11}$$

where V is the total worn volume, s is the total sliding distance, and P is the normal load. Here, the dimensional Archard wear coefficient $k = K/H$ is used as the proportionality constant to the pressure p times the sliding distance s, as shown in Eq. (2).

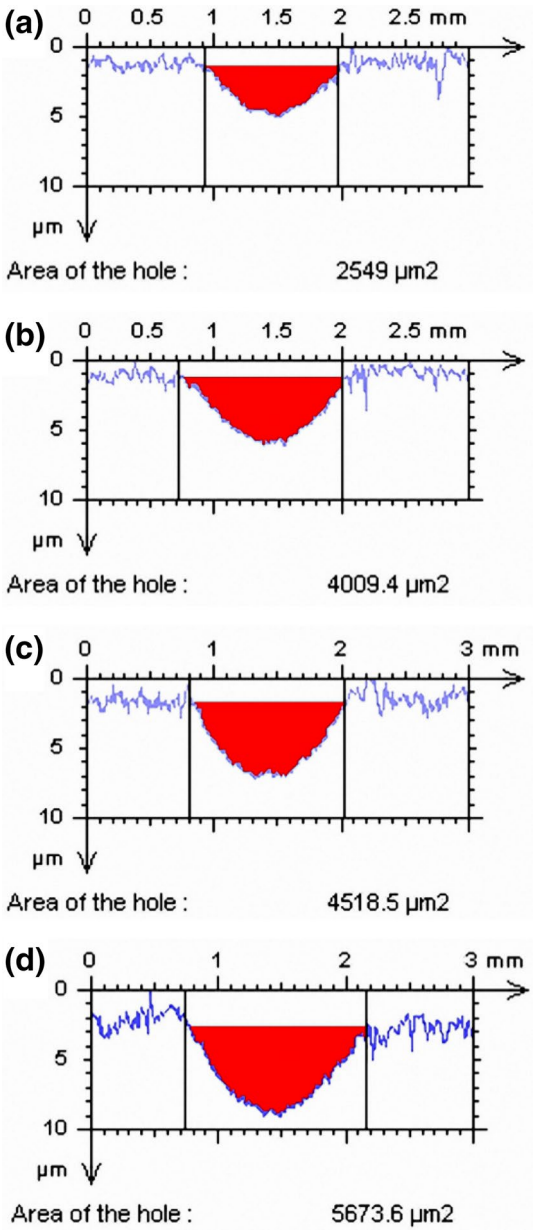

Fig. 7 Profiles of worn blocks for the sliding distances of 31 m (**a**), 77 m (**b**), 155 m (**c**), and 233 m (**d**)

4 Results

4.1 Surface Topography Evolution

In this study, the steel cylinder and epoxy resin block were used as the friction counterpart. The sliding line contact was composed of the cylindrical surface and the block.

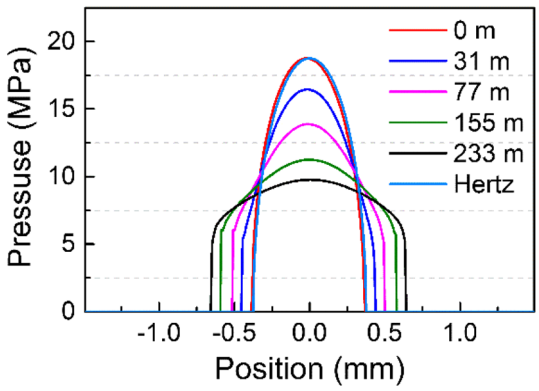

Fig. 8 Evolution of the contact pressure in the simulation under different sliding distances

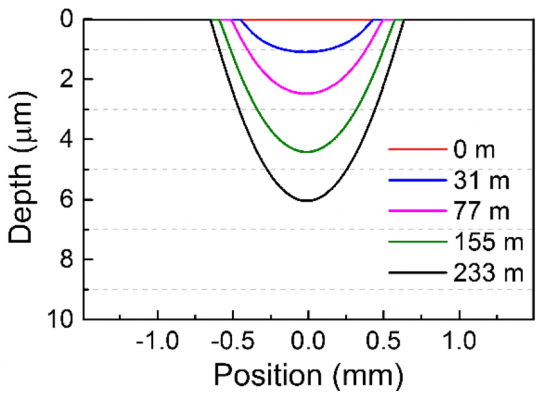

Fig. 9 Wear scar evolution of the block in the simulation under different sliding distances

Owing to the obvious difference between the hardness of the friction pairs, the cylinder was treated as a rigid body, and therefore the wear occurred solely on the block. The three-dimensional wear scar after running 155 m is shown in Fig. 6. It seemed that non-conforming contact changed into conforming contact during the wear processes. Figure 7 displays wear scars obtained with the help of TalyMap from cross-sections perpendicular to the sliding direction and worn volume under 31, 77, 155, and 233 m sliding distances. The wear coefficient was estimated to be 2×10^{-9} MPa^{-1} using Eq. (11).

4.2 Pressure and Wear Scar Evolution

The simulation was carried out after the desired parameters were obtained. The evolution of contact pressure in the simulation is shown in Fig. 8. The maximum contact pressure and contact width were 18.75 MPa and 0.758 mm, respectively, consistent with the Hertz solution. The maximum contact pressure decreased gradually, while the contact width showed the opposite trend with the increase in sliding distance. The contact pressure tended to be evenly distributed when the sliding distance increased to a certain value; this trend became more obvious as the sliding distance continued to increase. Figure 9 shows the evolution of surface profiles in the simulation. This figure indicates that the maximum wear depth increases gradually when the sliding distance increases.

4.3 Photoelastic Pattern

The examples of the isochromatic patterns near the contact surfaces are shown in Fig. 10; the area of interest is 4 mm × 3 mm. Figure 10a, c shows the experimental results. As shown in these images, the maximum fringe order occurs inside the body within a small distance from the contact surface. Figure 10a shows the fringe pattern at static contact. An eccentric fringe pattern, shown in Fig. 10c, was observed when the two bodies were about to slide against each other, which is consistent with the theoretical results [23]. Simultaneously, simulation results at static contact and initial sliding are shown in Fig. 10b, d.

Figure 11 shows the experimental and simulation results of photoelastic patterns during wear processes. As the sliding distance increases, the wear volume of the block also increases. From the experimental results, it can be observed that the enclosed area of the maximum fringe order declined as the wear volume increased.

5 Discussion

Using photoelasticity to observe the sliding distance variant plane stress has enabled this novel study. Additionally, experimental results were compared with numerical simulations. The main results are presented; first, a block-on-cylinder contact wear tester was placed in a circular polariscope, which allowed us to use a CCD camera to capture the in situ sliding distance variant isochromatic pattern of the block during wear, and, second, numerical simulations were conducted in the framework of the CGM method and Archard's wear law. Wear processes were quantified by analyzing profiles and measuring wear volumes from the wear test. The photoelastic results qualitatively illustrated the evolution of the maximum shear stress in the subsurface during the wear processes.

Figures 7 and 9 show the experimental and simulation results of the wear profiles with different sliding distance. Comparing the two figures, it can be seen that there is a large gap between the wear volumes when the relative sliding distance is small. The main reason is that the surface roughness will affect the measurement results when

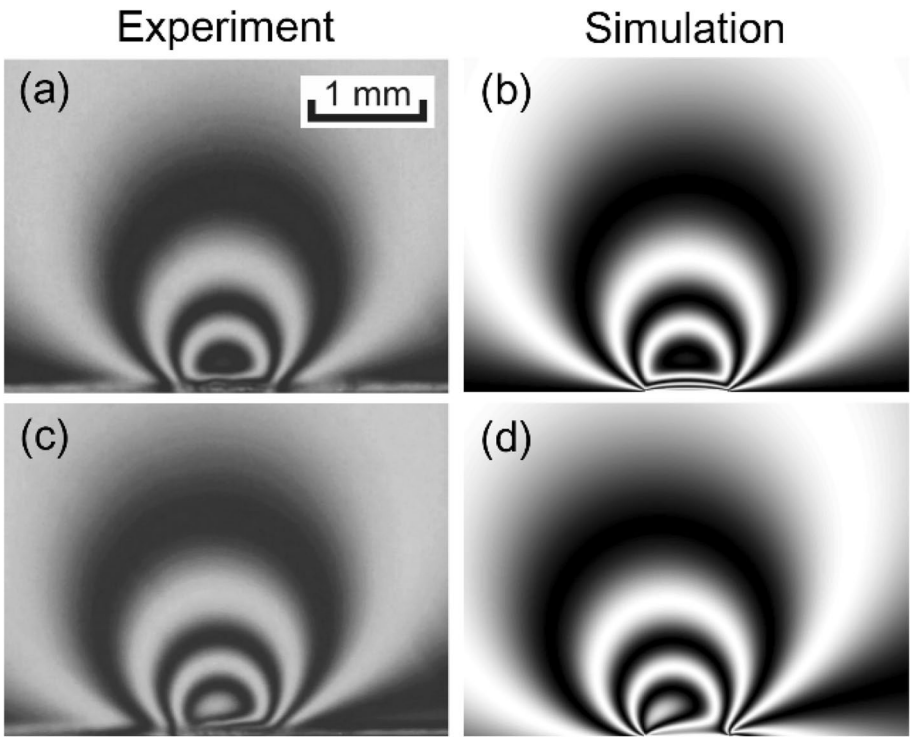

Fig. 10 Photoelastic patterns of static contact and initial sliding for the experiment (**a, c**) and the simulation (**b, d**)

the wear distance is small, which affects the accuracy of wear volume measurements. Figure 8 shows the evolution of normal contact pressure at different sliding distances. According to the results of Ref. [11, 26], the center of the contact strip will be displaced from the axis of symmetry when two different elastic bodies come into contact and will eventually become symmetrical with the existence of wear. However, these trends are not obvious in Fig. 8 due to the low friction coefficient.

The photoelastic patterns in static contact shown in Fig. 10a, b are similar, while at the initial sliding stage the inclination angle of the maximum order fringe is larger than the experimental results (shown in Fig. 10c, d). The inclination angle is influenced by the tangential force. In this study, the Coulomb friction law was employed to calculate the tangential force; however, the relationship between normal and tangential forces is more complicated [27]. In addition, it can be observed from Fig. 5 that the friction coefficient is a time-variant value. At the beginning of macro sliding, the friction coefficient is smaller than 0.25, which is the value used in this paper. Every factor mentioned above might cause differences between the theoretical and experimental results. Due to the wear volume differences between the experiment and simulation, the isochromatic patterns will inevitably be different. However, it could also partially explain the trend of the maximum shear stress in the subsurface. At this point, there are still difficulties separating principal stress directly from the isochromatic patterns under dynamic conditions. Figure 12 shows shear stress evolution near the contact surfaces by the simulation method. This method reproduces the value and position of the maximum shear stress during wear processes. As the wear volume increases, the value of the maximum shear stress gradually decreases. Additionally, the maximum shear stress position transferred from the subsurface to the edge of the contact region.

It is noted that, in the simulation method, the mathematical treatment for the tangential force is classical, i.e., it assumes a constant friction coefficient. However, the friction coefficients vary with time, which will influence the photoelastic patterns. In addition, Archard's wear law was employed to calculate wear volumes; nonetheless, hundreds of wear laws have been developed that are suitable for different occasions [13]. Furthermore, the quarter-wave plate can be used for only one specific wavelength due to its nature. This will lead to the fact that the emitted light is not a circularly polarized light in the strict sense but an elliptically polarized light. A broader investigation regarding the involvement of these effects on the results will be the focus of future research.

6 Conclusions

The photoelastic method was applied to observe in situ plane stress during wear in a line contact. As there are still some difficulties in separating principal stress directly from the

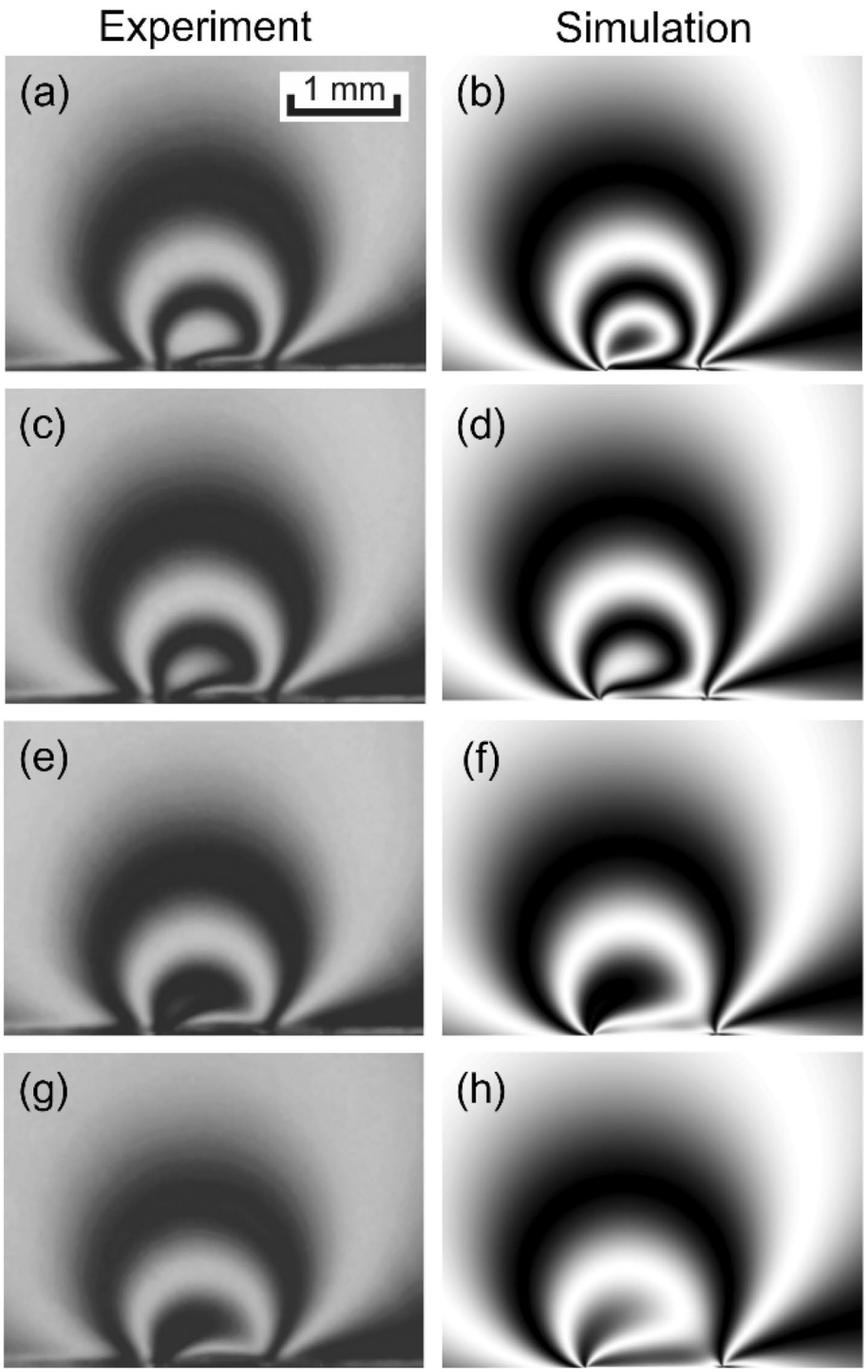

Fig. 11 Photoelastic patterns for the experiment and the simulation, respectively, after running 31 m (**a, b**), 77 m (**c, d**), 155 m (**e, f**) and 233 m (**g, h**)

isochromatic patterns under dynamic conditions, numerical simulation was also conducted in this study. The main conclusions were as follows:

a. The photoelastic technique was employed to observe real-time isochromatic patterns, which can qualitatively illustrate the evolution of the maximum shear stress during wear processes in a line contact.
b. The normal contact pressure was computed by the CGM algorithm for arbitrary contact profiles, and the Archard's wear law was applied to calculate wear volumes.
c. Based on the numerical results of wear, the photoelastic patterns were simulated and compared to the experimental results. In addition, the value and position of the maximum shear stress were computed. The simulation results

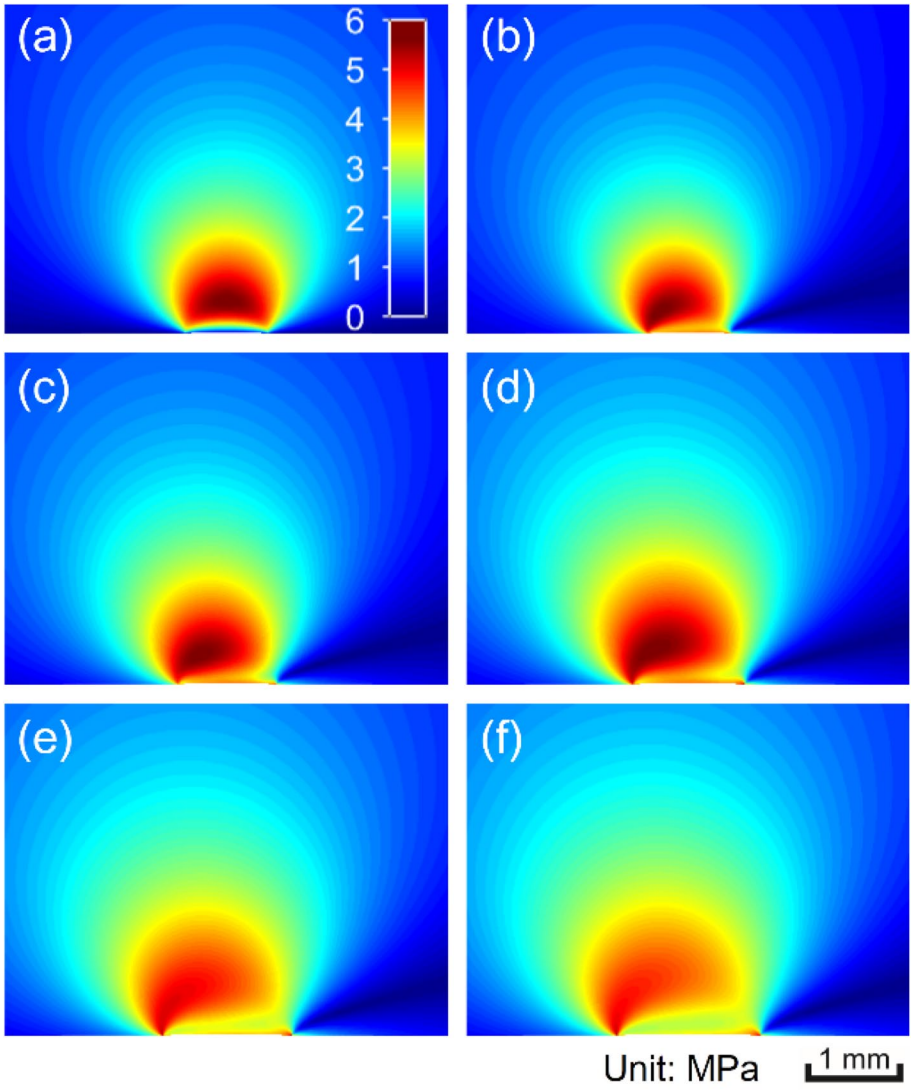

Fig. 12 Shear stress evolution with sliding distance: static contact (**a**), initial sliding (**b**), 31 m (**c**), 77 m (**d**), 155 m (**e**), and 233 m (**f**)

showed that as the wear volume increased, the value of the maximum shear stress decreased gradually. Additionally, the maximum shear stress position transferred from the subsurface to the edge of the contact region.

Acknowledgements The authors would like to acknowledge the financial support of the National Natural Science Foundation of China (Grant No. 51575190).

Appendix A

The surface deflection distribution produced by a given contact pressure $p(x)$ is shown in Eq. (1). As the 'rigid-body' approach δ in Eq. (5) can be determined based on the load balance condition, the constant C in Eq. (1) can be merged with it. Equation (1) can be expressed as the Green function:

$$u = -\int_{I_g} K(x - x')p(x')\mathrm{d}x', \tag{A.1}$$

where I_g is the grid area and $K(x)$ represents the surface displacement distribution produced by a unit concentrated normal force acting at the origin. Comparing Eq. (A.1) with (1), the kernel $K(x)$ is given by

$$K(x) = \frac{2}{\pi E^*}\ln|x| + \frac{\mu}{2G^*}H(x), \tag{A.2}$$

where $H(x)$ is the Heaviside step function. Under the assumption of stepwise constant distribution of contact pressure, the influence coefficient K_{i-j} is given by

$$K_{i-j} = \int_{x_j-\Delta x/2}^{x_j+\Delta x/2} \frac{2}{\pi E^*}\ln|x' - x_i| + \frac{\mu}{2G^*}H(x' - x_i)\mathrm{d}x'. \tag{A.3}$$

Integrating Eq. (A.3) yields an explicit formula for K_{i-j}, which can be expressed as

$$K_{i-j} = \frac{2}{\pi E^*}\left[f\left(\left|x_i - x_j\right| + \Delta x/2\right) - f\left(\left|x_i - x_j\right| - \Delta x/2\right)\right] + \frac{\mu \Delta x}{2G^*} H\left(x_j - x_i\right), \tag{A.4}$$

where $f(x) = x(\ln|x| - 1)$.

Appendix B

$$N_{i-j}^{rs}\left(z_k\right) = n^{rs}\left(x_i - x_j + \Delta x/2, z_k\right) - n^{rs}\left(x_i - x_j - \Delta x/2, z_k\right)$$
$$T_{i-j}^{rs}\left(z_k\right) = t^{rs}\left(x_i - x_j + \Delta x/2, z_k\right) - t^{rs}\left(x_i - x_j - \Delta x/2, z_k\right), \tag{B.1}$$

where

$$n^{xx}(x,z) = \frac{1}{\pi}\left[\frac{xz}{x^2+z^2} - \arctan\left(\frac{x}{z}\right)\right]$$
$$n^{zz}(x,z) = \frac{1}{\pi}\left[-\frac{xz}{x^2+z^2} - \arctan\left(\frac{x}{z}\right)\right]$$
$$n^{xz}(x,z) = \frac{1}{\pi}\frac{z^2}{x^2+z^2}$$
$$t^{xx}(x,z) = \frac{1}{\pi}\left[-\frac{z^2}{x^2+z^2} - \ln\left(x^2+z^2\right)\right]$$
$$t^{zz}(x,z) = \frac{1}{\pi}\frac{z^2}{x^2+z^2}$$
$$t^{xz}(x,z) = \frac{1}{\pi}\left[\frac{xz}{x^2+z^2} - \arctan\left(\frac{x}{z}\right)\right].$$

References

1. Marshall, D.B., Shaw, M.C., Morris, W.L.: Measurement of interfacial debonding and sliding resistance in fiber reinforced intermetallics. Acta Metall. Mater. **40**(3), 443–454 (1992). https://doi.org/10.1016/0956-7151(92)90392-R
2. Hu, Z., Lu, W., Thouless, M.D.: Slip and wear at a corner with Coulomb friction and an interfacial strength. Wear. **338–339**, 242–251 (2015). https://doi.org/10.1016/j.wear.2015.06.010
3. Dally, J.W., Chen, Y.M.: A photoelastic study of friction at multipoint contacts. Exp. Mech. **31**(2), 144–149 (1991). https://doi.org/10.1007/BF02327567
4. Bryant, M.D., Jau-Wen, L.: Photoelastic visualization of contact phenomena between real tribological surfaces, with and without sliding. Wear. **170**(2), 267–279 (1993). https://doi.org/10.1016/0043-1648(93)90247-J
5. Burguete, R.L., Patterson, E.A.: A photoelastic study of contact between a cylinder and a half-space. Exp. Mech. **37**(3), 314–323 (1997). https://doi.org/10.1007/BF02317424
6. Fang, Y., He, J., Huang, P.: Experimental and numerical analysis of soft elastohydrodynamic lubrication in line contact. Tribol. Lett. **65**(2), 42 (2017). https://doi.org/10.1007/s11249-017-0825-9
7. Fernández, M.S.-B., Calderón, J.M.A., Díez, P.M.B., Segura, I.I.C.: Stress-separation techniques in photoelasticity: a review. J. Strain Anal. Eng. Des. **45**(1), 1–17 (2009). https://doi.org/10.1243/03093247JSA583
8. Solaguren-Beascoa Fernández, M.: Data acquisition techniques in photoelasticity. Exp. Tech. **35**(6), 71–79 (2011). https://doi.org/10.1111/j.1747-1567.2010.00669.x
9. Yoneyama, S., Arikawa, S., Kobayashi, Y.: Linear and nonlinear algorithms for stress separation in photoelasticity. Exp. Mech. **52**(5), 529–538 (2012). https://doi.org/10.1007/s11340-011-9512-1
10. Narayanamurthy, C.S., Pedrini, G., Osten, W.: Digital holographic photoelasticity. Appl. Opt. **56**(13), F213-F217 (2017). https://doi.org/10.1364/AO.56.00F213
11. Zhan, W., Huang, P.: Numerical analysis of time-varying wear with elastic deformation in line contact. Friction (2018). https://doi.org/10.1007/s40544-017-0195-1
12. Andersson, J., Almqvist, A., Larsson, R.: Numerical simulation of a wear experiment. Wear. **271**(11–12), 2947–2952 (2011). https://doi.org/10.1016/j.wear.2011.06.018
13. Meng, H., Ludema, K.: Wear models and predictive equations: their form and content. Wear. **181**, 443–457 (1995). https://doi.org/10.1016/0043-1648(95)90158-2
14. Archard, J.: Contact and rubbing of flat surfaces. J. Appl. Phys. **24**(8), 981–988 (1953). https://doi.org/10.1063/1.1721448
15. Hegadekatte, V., Huber, N., Kraft, O.: Finite element based simulation of dry sliding wear. Modell. Simul. Mater. Sci. Eng. **13**(1), 57–75 (2004). https://doi.org/10.1088/0965-0393/13/1/005
16. Mukras, S., Kim, N.H., Sawyer, W.G., Jackson, D.B., Bergquist, L.W.: Numerical integration schemes and parallel computation for wear prediction using finite element method. Wear. **266**(7), 822–831 (2009). https://doi.org/10.1016/j.wear.2008.12.016
17. Hu, Z., Lu, W., Thouless, M.D., Barber, J.R.: Simulation of wear evolution using fictitious eigenstrains. Tribol. Int. **82**, 191–194 (2015). https://doi.org/10.1016/j.triboint.2014.10.015
18. Arjmandi, M., Ramezani, M., Giordano, M., Schmid, S.: Finite element modelling of sliding wear in three-dimensional woven textiles. Tribol. Int. **115**, 452–460 (2017). https://doi.org/10.1016/j.triboint.2017.06.015
19. Flodin, A., Andersson, S.: Simulation of mild wear in spur gears. Wear. **207**(1–2), 16–23 (1997). https://doi.org/10.1016/S0043-1648(96)07467-4
20. Põdra, P., Andersson, S.: Wear simulation with the Winkler surface model. Wear. **207**(1), 79–85 (1997). https://doi.org/10.1016/S0043-1648(96)07468-6
21. Sfantos, G., Aliabadi, M.: Wear simulation using an incremental sliding boundary element method. Wear. **260**(9), 1119–1128 (2006). https://doi.org/10.1016/j.wear.2005.07.020
22. Polonsky, I.A., Keer, L.M.: A numerical method for solving rough contact problems based on the multi-level multi-summation and conjugate gradient techniques. Wear. **231**(2), 206–219 (1999). https://doi.org/10.1016/S0043-1648(99)00113-1
23. Johnson, K.L.: Contact mechanics. Cambridge University Press, Cambridge (1985)
24. Theocaris, P.S., Gdoutos, E.E.: Matrix theory of photoelasticity, vol. 11. Springer, Berlin (1979)
25. Lei, Z., Yun, H., Zhao, Y., Pan, X.: Automatic determination of fringe constant in digital photoelasticity. Eng. Mech. **26**(12), 40–45 (2009)
26. Zhan, W., Huang, P.: Numerical analysis of elastic wear in line contact. J. South China Univ. Technol. **45**(5), 45–51 (2017). https://doi.org/10.3969/j.issn.1000-565X.2017.05.007
27. Mo, Y., Turner, K.T., Szlufarska, I.: Friction laws at the nanoscale. Nature. **457**(7233), 1116–1119 (2009). https://doi.org/10.1038/nature07748